Dataset of DInSAR wrapped phase signals for AI-based automated detection and classification of mass movements

Cristina Reyes-Carmona[1], Alessandro Mercurio[2], Alessandro Mondini[3], Fabio Bovenga[4], Alessandro Simoni[2], Federico Agliardi[1]

[1]Department of Earth and Environmental Sciences, University of Milano-Bicocca, Milan, 20126, Italy
[2]Department of Biological, Geological and Environmental Sciences, University of Bologna, Bologna, 40126, Italy
[3]Istituto di Matematica Applicata e Tecnologie Informatiche, Consiglio Nazionale delle Ricerche (CNR-IMATI), Genoa, 16149, Italy
[4]Istituto per il Rilevamento Elettromagnetico dell'Ambiente, Consiglio Nazionale delle Ricerche (CNR-IREA), Bari, 70126, Italy

Corresponding author: Cristina Reyes-Carmona, cristina.reyescarmona@unimib.it

Abstract

With the growing use of Artificial Intelligence (AI) in remote sensing of mass movements, available datasets for model training and validation are increasingly needed. Although Differential Synthetic Aperture Radar Interferometry (DInSAR) is a widely used technique for studying mass movements, wrapped interferograms remain less exploited, and the importance of geomorphological expertise in their interpretation is not usually emphasised. In this work, we introduce a dataset of DInSAR wrapped phase signals designed to support the development of Deep Learning (DL) models for the automated detection and classification of active slow-moving mass movements. The dataset covers two selected areas in the Central European Alps and the Northern Apennines. It contains 4910 DInSAR wrapped phase signals derived from 92 Sentinel-1 interferograms with temporal baselines ranging from 6 days to 1 year, and classified into nine distinct landslide and periglacial landform classes after careful geomorphological interpretation. This dataset is expected to support the scientific community in AI-based applications for mass movement research, while also serving as a benchmark for the generation of comparable datasets.

Background & Summary

Slow mass movements are major drivers of mountain slope dynamics, which results from different mechanisms depending on the materials involved, geomorphic settings and external forcing (e.g., Korup et al., 2010). Alpine settings characterised by hard crystalline and sedimentary rocks and para/periglacial environments are extensively affected by deep-seated slope deformations and periglacial features such as rock glaciers. Conversely, mountain ranges with a fluvial-dominated topography in sedimentary weak rocks, such as the Apennines, are typically

affected by long-lived earthflows. These mass movements have distinct controlling factors and spatio-temporal patterns, threatening human life and infrastructure in different ways. Mitigating risks posed by mass movements requires capabilities to: a) detect and classify different active processes systematically and rapidly over wide areas; b) monitor their evolution towards possible destabilisation; and c) predict interactions with elements at risk.

The detection and classification of active mass movements rely on a combination of conventional geomorphological methods and a wide range of remote sensing techniques, both ground-based or space-borne (Guzzetti et al., 2012). Among these, multi-spectral, radar and lidar imaging techniques have been increasingly used and developed since the early 2000s (Casagli et al., 2023). In particular, Differential Synthetic Aperture Radar Interferometry (DInSAR) has emerged as one of the major breakthroughs for large-scale ground surface monitoring (Mondini et al., 2021), typically through long-term displacement time series derived from several interferograms (Ferretti et al., 2002; Berardino et al., 2003). However, applying multitemporal DInSAR techniques in mountainous regions remains challenging due to geometrical, spatial and temporal limitations inherent to these environments (Beckaert et al., 2020). Geometrical constraints arise from the SAR viewing geometry and visibility (Wasowski and Bovenga 2014), which are even more significant in steep terrain. Spatial issues include phase unwrapping errors as the result of large deformation gradients and complex deformation patterns, whereas temporal limitations are mainly related to coherence loss in fast-moving areas and in surfaces affected by seasonal snow or dense vegetation cover. In this context, wrapped interferograms derived from standard two-pass DInSAR techniques have shown promising potential for detecting mass movements in mountain environments, as these products can better deal with spatial and temporal decorrelation conditions (Crippa et al., 2020; Manconi, 2021). However, since interferograms provide only single snapshots of ground displacement, their use for signal detection involves analysing a large amount of interferograms (Dini et al., 2019), which is time-consuming and requires expert interpretation. For this reason, Deep Learning (DL) techniques have emerged to enhance and automate the interpretation of interferograms, reducing costs and improving analysis quality where the human eye struggles to identify relevant displacement patterns (Zhu et al., 2021).

Some initial investigations have already explored the application of DL using interferograms for detecting volcanic (Anantrasirichai et al., 2018; 2019; Hooper et al., 2021; Fadhillah et al., 2022) and co-seismic deformation (Brengman and Barnhart, 2021; Silva et al., 2022; Zhu et al., 2024), as well as ground subsidence (Rotter and Muron, 2020; He et al., 2024) and slow-moving landslides (Fu et al., 2022; Zhang et al., 2024). With this growing use of DL in ground motion detection, the development of well-documented training datasets becomes crucial to ensure process-sound and interpretable results. Few studies have provided open training datasets suited to this aim (Bountos et al., 2022; Bralet et al., 2024; Liu et al. 2025). Bountos et al., (2022) generated a dataset containing 2247 manually annotated displacement signals from wrapped interferograms related to earthquake-induced deformations and four different types of volcanic deformation. Liu et al., (2025) created a dataset of 1773 samples of interferometric signals associated with earthquake deformation, with event identification and labelling performed

through a semi-automatic workflow. Bralet et al., (2024) focused on slow-moving landslides and rock glaciers by generating a total of 8701 manually annotated patches from wrapped interferograms for DL-based semantic segmentation purposes. These authors also emphasised the importance of geomorphological expertise for the interpretation and annotation of interferograms. Taken together, these works evidence two clear needs: (1) additional open-access training datasets to support DL models intended for object detection and classification, and (2) guidelines on how to compile such datasets with consideration of geomorphology.

From this perspective, we present a dataset of DInSAR wrapped phase displacement signals associated with different classes of slow-moving mass movements, typical of diverse geological and geomorphological contexts. This dataset has been specifically designed to train DL object detectors models for the automated detection and classification of mass movements. The displacement signals were mapped using bounding boxes and compiled in two study areas, characterised by sharply different geological-geomorphological conditions and hosting diverse types of active mass movements: one sector in the Central Alps across Italy and Switzerland, and another in the Northern Apennines (Emilia-Romagna, Italy). By incorporating this complexity, we aim at building a more representative dataset to support the development of models with broader classification capabilities. The considered mass movement include different types of landslides (e.g., deep-seated gravitational slope deformations, rockslides, debris slides, earthflows and earthslides) as well as periglacial landforms such as rock glaciers and protalus ramparts in alpine areas. Our dataset is named MIRAGE (**M**ass movement **I**nvestigation and prediction through geomorphology, **R**emote sensing and **A**rtificial intelli**GE**nce), from the research project in which it was developed (see Fundings). Moreover, we describe our procedure for interpreting displacement signals, and illustrate the interferometric patterns associated with each identified mass movement type. By detailing our workflow, we aim to suggest some practical steps to construct similar datasets, while emphasising the essential role of expert geomorphological knowledge in correctly interpreting interferometric signals.

Study areas

We selected two geologically and geomorphologically distinct mountainous areas to build a representative dataset that includes diverse mass movement types: the Northern Apennines and the Central Alps (Fig. 1a). These areas were also selected to address challenges commonly found in DInSAR applications: (1) complex mountain terrain, where geometric distortions often limit radar visibility and where vegetation and snow cover can cause signal decorrelation; and (2) occurrence of mass movements characterised by different displacement rates and temporal trends (e.g., steady, seasonal/episodic, accelerating) (Crosta and Agliardi, 2003; Ronchetti et al., 2009; Zangerl et al., 2010; Crosta et al 2017; Bayer et al. 2017; Agliardi et al., 2020; Fey and Krainer, 2020), for which displacement signals may be difficult to detect and interpret. Overall, the Central Alps represent a typical high-mountain environment, where the landscape has been strongly conditioned by paraglacial and post-glacial processes,

resulting in U-shaped valleys with local relief often exceeding 1-1.5 km (Fig. 1b). In this region, most slope instabilities have been triggered by glacial debuttressing, while periglacial features are associated with remnants of post-glacial permafrost conditions. By contrast, the Apennines form a structurally complex mountain range, characterised by generally softer lithologies and a gentle landscape predominantly shaped by fluvial erosion and slope processes such as earthslides and earthflows (Fig. 1c).

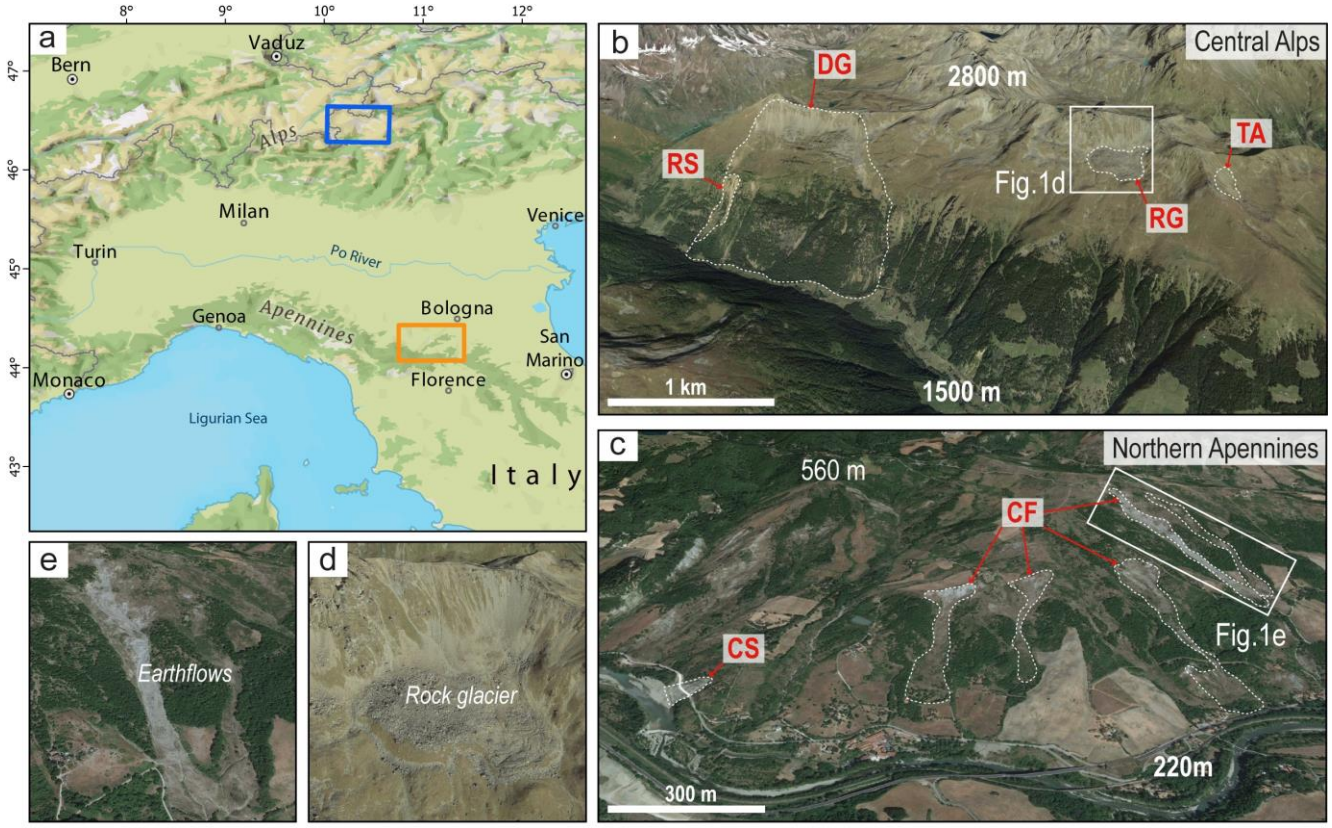

Figure 1. (a) Location of the study areas: the Central Alps (blue rectangle) and the Northern Apennines (orange rectangle). **(b)** Representative landscape view of the Central Alps with some of their typical mass movements: rockslides (RS), deep-seated gravitational slope deformations (DG), rock glaciers (RG) and talus deposits (TA). **(c)** Representative landscape view of the Northern Apennines, with some of their typical landslide types: earthslides (CS) and earthflows (CF). **(d)** Detailed view of a rock glacier in the Central Alps, outlined in Fig. 1b. **(e)** Detailed view of an earthflow in the Northern Apennines, outlined in Fig. 1c (a: map from ArcGIS Pro, b-e: images from Google Earth™).

Central Alps

The selected area extends over 1900 km² of the Central Alps, encompassing the Upper Valtellina (Lombardy, Italy) and adjacent regions of Trentino-Alto Adige/Südtirol (Italy) and Grisons (Switzerland) (Fig. 1a), with elevations ranging from 590 m to nearly 3900 m.a.s.l. The region is characterised by a high-mountain climate, with persistent snow cover during winter and spring above 1200-1500 m, and permafrost potentially occurring above between 2600 and 3000 m (Boeckli et al., 2012). The main lithologies are moderately strong metamorphic rocks that include

phyllites, micaschists and paragneisses, followed by other minor lithologies such as granitoids, carbonates and flysch rocks (Conti et al., 1994; Froitzheim et al., 1994; Froitzheim and Manatschal, 1996). Regional inventories available in Lombardy include 5431 landslides of various typologies (IFFI, 2017), with a total area of 308 km², and 76 Deep-Seated Gravitational Slope Deformations (DSGSDs) (Agliardi et al., 2013; Crosta et al., 2013; Crippa et al., 2021), covering 251 km². There are also regional inventories of rock glaciers in Lombardy (Scotti et al., 2013) and Alto-Adige (INSPIRE Geoportal, 2010), covering a total area of 45 km^2. In this alpine area, the main slope movement types are slow rock-slope deformations that include DSGSDs and large landslides (mainly rockslides) that can evolve independently or nucleate within DSGDGs (Fig. 1b). These slope movements are constrained by inherited tectonic structures and are further promoted by stress and hydrological perturbations related to deglaciation (Crosta et al., 2013; Gramiger et al., 2017; Riva et al., 2018; Agliardi and Crippa, 2022). Although typically slow (mm/yr), these deformations can accelerate rapidly and eventually lead to catastrophic failures (Crosta et al., 2004). On the other hand, permafrost degradation in periglacial environments has influenced the development of other types of mass movements in the area, such as rock glaciers and protalus ramparts (Fig. 1b, d), which can reach high movement rates (m/yr) (Cicoira et al., 2021; RGIK, 2023; Agliardi et al., 2025; Crippa et al., 2025; Brardinoni et al., 2026). Based in previous inventories, the mass movements considered in this study were the following six types: deep-seated gravitational slope deformation (DG), debris slide (DS), rockslide (RS), rock glacier (RG), protalus rampart (PR) and talus (TA).

Northern Apennines

The selected area spans around 1200 km^2 within the Reno River basin, southwest of Bologna (Emilia-Romagna, Italy) (Fig. 1a), where elevations range from 60 to 1365 m.a.s.l. The climate is Mediterranean, with 1300-1400 mm/yr precipitation concentrated in spring and autumn, driving peak landslide activity in late winter and early spring (Tomozeiu et al., 2000; Pavan et al., 2008). The geological setting is dominated by clay-rich formations, such as clay-shales and marls, as well as by turbiditic flysch units (Ricci Lucchi, 1986; Pini, 1999). Landslide types found across the area are strongly governed by lithological conditions. Fine-grained formations, particularly clay-shales, are prone to instability due to their weak geotechnical properties. In these terrains, earthflows are widespread (Simoni et al., 2013) (Fig. 1c, e) and show a typical flow-like morphology originating from repeated reactivations. Velocities typically range from very slow to extremely slow (mm/yr to cm/yr) during the dormant phase (which can last hundreds of years) to meters per hour during a catastrophic failure (Bertello et al., 2018). In many instances, the failure mechanisms, originating as a slide, evolve downslope transforming into a flow and result in complex landslide processes (Borgatti et al., 2006; Corsini et al., 2006; Berti et al., 2017). Conversely, flysch terrains host large translational or rotational slides (Berti et al., 2017) and localised rockfalls depending on the slope geometry. According to the regional landslide inventory (RER, 2024), over 11900 active or dormant landslides are mapped in the selected study area. The landslide index (ratio between the area covered by landslide deposits and the

outcropping area of each bedrock type) confirms the strong lithological control, with highest densities observed in clay-shales (39%) and pelitic flysch (33%) formations and densities around 10% of tertiary sandstones/marls. Guided by previous inventories, the landslides considered in this study are classified as follows: earthflows in clay-shales (CF), earthslides in shales/marls (CS) and rockslides in flysch rocks (FS).

Methods

The MIRAGE dataset consists of a collection of wrapped SAR interferograms in which displacement signals associated with mass movements have been recognised, and a corresponding set of manually generated bounding box annotations, specifically designed for training object detection DL models. Recent advances in artificial intelligence model architectures, including Convolutional Neural Networks (CNN), transformer-based detectors, and object detection frameworks like YOLO, Faster R-CNN and RetinaNet have demonstrated a strong capability for identifying deformation patterns in remote sensing imagery (Li et al., 2022; Zhang et al., 2023; Gui et al., 2024; Coulson et al., 2025). The following sections describe in detail: (1) the DInSAR processing workflows used to generate the interferograms for both study areas; (2) the criteria used to constrain the geomorphological classification of the phase signals identified in the wrapped SAR interferograms; and (3) the step-by-step procedure adopted for the identification, annotation and classification of displacement signals according to their associated type of mass movement.

Satellite-based DInSAR

DInSAR processing was carried out independently for each of the two study areas, adopting consistent parameters such as pixel resolution (i.e., ground sampling distance), coordinate system, and spatial coverage to ensure dataset comparability. For the Northern Apennines, the processing was performed using GMTSAR (Sandwell et al., 2011), whereas SARscape® (Sarmap SA) was employed for the Central Alps. In both cases, we used C-band Sentinel-1 satellite images acquired in Interferometric Wide Swath (IW) mode and Single Look Complex (SLC) format, with a minimum revisit time of six days (Table 1). Interferograms were then generated using image pairs with different temporal baselines (i.e., the time interval between acquisitions) (Table 1) and kept in phase format modulo 2π (i.e., wrapped interferograms). Importantly, the same filtering and coherence estimation procedures were applied across both processing chains, ensuring that the resulting interferograms exhibit comparable noise characteristics and thus guaranteeing the homogeneity of the final dataset.

GMTSAR (Generic Mapping Tools SAR) is a widely used open-source SAR/DInSAR processing software to process satellite data, allowing the generation of multiple products from complex interferograms to LOS displacement. The processing methodology involved a series of sequential steps, beginning with the acquisition of Sentinel-1 SAR images. In this case all selected images, for both ascending and descending orbits, were acquired

between January 2016 and April 2025 (Table 1). All downloaded SAR images were co-registered to a single master acquisition, chosen from the temporal centre of them. The subsequent projection of a digital elevation model into radar geometry enabled the subtraction of the topographic phase component, isolating ground displacement signals. The wrapped interferograms were then formed by combining pairs of these co-registered images at five different temporal baselines (Bt): 6, 12, 18, 24 and 30 days (Table 1). Longer baselines were not considered, as it was consistently observed during preliminary analysis that those interferograms exhibited an insufficient signal-to-noise ratio, which hindered the reliable interpretation of displacement signals. Coherence maps were also produced, using a Boxcar filter and offering insight into image quality and the reliability of the phase information. To mitigate noise and enhance the deformation signals, interferograms were then filtered using a combination of Gaussian and Goldstein filters (Goldstein and Werner, 1998). The final step involved geocoding and exporting the wrapped interferograms to TIFF format for their use in a GIS environment.

Study area / **Parameter**	**Northern Apennines**	**Central Alps**
Acquisition mode	Interferometric Wide Swath (IW)	
Product type	Single Look Complex (SLC)	
Maximum revisit time (days)	6	
Orbits processed	Ascending, descending	
Track	117 (ascending), 95 (descending)	15 (ascending), 168 (descending)
Temporal span of SAR images	January 2016 – April 2025	June 2018 - September 2021
Number of processed interferograms	1042 (585 ascending, 457 descending	203 (85 ascending, 118 descending)
Bt of processed interferograms (days)	6, 12, 18, 24, 30	6, 12, 30, 60, 90, 365
Interferogram GSD resolution (m)	15 x 15	

Table 1. Details of the Sentinel-1 SAR images and interferograms processed for each study area (Bt: temporal baseline, GSD: ground sampling distance).

SARscape is a commercial software implemented as a toolbox in ENVI (version 6.1.0) that allows interferometric SAR processing in both dual-pass (interferograms) and multi-temporal modes (persistent scatterers time series). For the interferogram generation, images and orbit files are first downloaded and then imported over the specific region of interest. The interferograms were then generated following a rolling pair strategy, in which each interferogram was created by pairing one image with a subsequent image at a fixed temporal baseline. The master image is progressively shifted forward in time, resulting in a continuous series of interferograms that capture temporal changes throughout the observation period. In this case, we used images from both ascending and

descending orbits, acquired from June 2018 to September 2021, only between June and September of each year to avoid snow coverage periods (Table 1). Interferograms were then generated at six different temporal baselines: 6 and 12 days; 1, 2, and 3 months; and 1 year (Table 1). These baselines were selected based on previous studies that highlighted their suitability for detecting these mass movements over the same area (e.g., Crippa et al., 2020; Agliardi et al., 2025). Subsequently, an adaptive filter was applied to reduce phase noise and coherence was generated using a Boxcar filter. The final steps included geocoding and extracting the phase component from the complex images, followed by export in TIFF format for GIS applications.

Geomorphological data

A comprehensive compilation of geomorphological data for the analysed mass movement processes, leveraging optical, topographic, and inventory data, is essential to properly interpret DInSAR wrapped phase signals associated with different classes of mass movements. Geomorphological information enables distinguishing true deformation patterns from artifacts and supports their classification into specific mass movement types. To this end, we used available mass movement inventories, high-resolution orthophotos, and DEM-derived products.

Regarding the inventory datasets, for the Central Alps, landslides were compiled from the Italian Landslide Inventory (IFFI, 2024), along with deep-seated gravitational slope deformations (DSGSDs) mapped in previous studies (Agliardi et al., 2013; Crippa et al., 2021). Rock glacier inventories were sourced from Scotti et al. (2013) for the Lombardy region and from the INSPIRE Geoportal (2010) for the Alto Adige region. For the Apennines area, we used landslide data from the Emilia-Romagna Regional Inventory (RER, 2024) and the Italian Landslide Inventory (IFFI, 2024). For both areas, orthophotos (years 2020-2024) and DEMs (5-10 m resolution), consistent with the time periods covered by the interpreted interferograms, were retrieved from the respective Italian regional geoportals: Emilia-Romagna (https://geoportale.regione.emilia-romagna.it/), Lombardia (https://www.geoportale.regione.lombardia.it/), Trentino (http://www.territorio.provincia.tn.it/) and Alto-Adige (https://natura-territorio.provincia.bz.it/). Different morphometric variables such as hillshade, aspect, slope, curvature, Terrain Roughness Index (TRI) and Topographic Wetness Index (TWI) were derived from the DEMs of each study area using SAGA GIS. These data were handled in a GIS environment for spatial visualisation, in which the GIS World Imagery (year 2022) was also used. Additionally, Google Earth™ historical imagery (2016-2022) was used for complementary 3D terrain exploration. The collected information was ultimately used to validate the morphological consistency of the deformation signals during the interpretation of the wrapped interferograms, as further explained in the following section. Finally, the distributions of the morphometric variable values within and outside mapped active domains belonging to different mass movement classes were compared to provide supporting information.

Interferogram interpretation and labelling

The interpretation and labelling of wrapped interferograms require both technical expertise in DInSAR and a solid understanding of the geomorphological processes under study. Before any interpretation, we carefully selected suitable interferograms. Although a coherent interferometric signal may be present, interferograms can still contain unwanted residual noise resulting from DEM inaccuracies, orbital errors, atmospheric phase delays, or temporal decorrelation (Zebker et al., 1997; Fattahi and Amelung, 2015). After proper interferogram selection, we carried out the labelling process. Creating a dataset of accurately labelled signals required a systematic manual annotation process, that combines the recognition of real interferometric displacement signals with the visual exploration of geomorphological features, both essential for a correct interpretation. This process consisted of the following steps (Fig. 2):

(0) Selection of optimal interferograms. Starting from more than 1200 interferograms processed over both areas, only 7% were interpreted to ensure the highest possible quality. Interferograms that displayed clear and consistent displacement signals were retained, while those dominated by decorrelation or atmospheric disturbances were discarded. This assessment relied on an initial visual inspection rather than specific coherence thresholds, with the signal-to-noise ratio estimated from the proportion of the interferogram displaying clear signal versus areas affected by decorrelation.

(1) Identification of DInSAR wrapped-phase signals on the interferograms. In this first stage, wrapped interferograms were systematically visually inspected to detect wrapped-phase difference patterns or fringes, indicating surface displacement standing out from the background. These patterns provide the first evidence of potential true ground displacement (Fig. 2).

(2) Verification of morphological consistency of interferometric signals. These potential displacement signals were then evaluated for morphological consistency using and inventories, topographic maps, orthophotos, Google Earth imagery, hillshade maps and other DEM-derived maps (slope, ruggedness, etc) (Fig. 2). This step allowed distinguishing signals related to mass movements from geometric artifacts, atmospheric, topographic phase residuals or noise caused by spatial and/or temporal decorrelation. Other interferometric products, such as coherence and radar visibility maps, can also be consulted at this stage. It is important to remark that this stage involved careful manual inspection performed by experienced geomorphologists, who relied on visual assessment of features such as the shape and continuity of wrapped-phase patterns across the terrain. Such a visual exploration approach plays a key role in this process, as highlighted in previous works that emphasise the importance of expert-based interpretation for identifying geomorphic patterns in remote sensing imagery (e.g., Guzzetti et al., 2012; Santangelo et al., 2022).

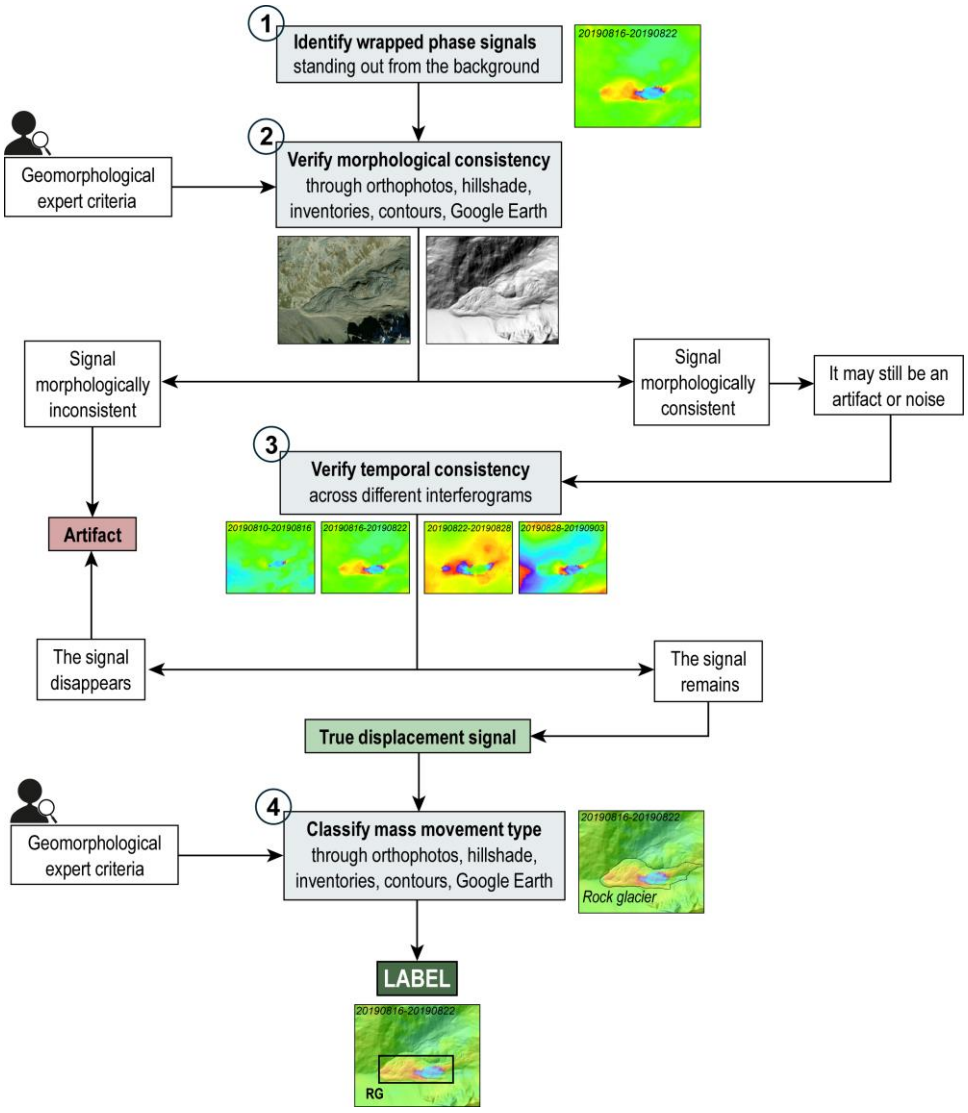

Figure 2. Flowchart of the labelling procedure for identification and classification of mass movements from wrapped interferograms.

(3) Verification of temporal consistency across different interferograms. This step is optional for cases when the signal is morphologically consistent, but some uncertainty may still remain. Such uncertainty can be related to the presence of vegetation, irregular signal shape, unusually small or large signal, or difficult recognition due to widespread surrounding phase noise. To discard that the signal corresponds to an artifact, we recommend a second verification of the signal by checking its temporal recurrence across multiple interferograms (Fig. 2). In this context, temporal recurrence is defined as the visibility of deformation signals in more than one interferogram. Since the analysed mass movements display long-term deformation behaviour, although with episodic or seasonal

reactivations or accelerations, these are commonly active at multiple temporal scales, thus being manifested in multiple interferograms at different baselines. Consequently, the probability of observing consistent signals in several interferograms, at least of the same baseline, is high in the case of true displacement. Therefore, temporal recurrence of a signal in at least two interferograms is suggested as an additional interpretative criterion whenever required.

(4) Classification of mass movement class. Finally, the true displacement signals were classified according to the type of mass movement. This classification relied again on expert geomorphological criteria, using the same products described in stage 2 (inventory, imagery, DEM-derived products, etc). Once confirmed as representing actual mass movements, the whole signals were enclosed in north-south oriented bounding boxes (rectangular polygons) as shapefiles in a GIS environment. To each bounding box, six attributes were assigned to then generate the so-called “label” (Fig. 2).

Three of these attributes describe the interferogram to which the signal is related: the acquisition dates, the temporal baseline and the orbit geometry. The other three attributes characterise the displacement signal: the signal quality, the uncertainty of the mass movement classification and, most importantly, the type of mass movement. The signal quality attribute indicates the clarity and distinctness of the interferometric signal. A value of 1 indicates high quality, characterised by well-visible signal patterns that clearly stand out from the background. A value of 2 denotes lower quality, typically occurring when the signal is slightly affected by decorrelation, which makes recognition more difficult, but it is still a clear true displacement signal. The uncertainty attribute represents the confidence level in the classification of the mass movement type. A value of 1 indicates low uncertainty, meaning the expert was highly confident in the assigned movement type, while a value of 2 denotes higher uncertainty, indicating that the classification was more ambiguous or less well-supported by the available data. Finally, the class attribute indicates the type of mass movement for each signal, following the nine types mentioned in the previous section: in the Alps, deep-seated gravitational slope deformation (DG), debris slide (DS), rockslide (RS), rock glacier (RG), protalus rampart (PR), and talus (TA); in the Apennines, earthflow in clay-shales (CF), earthslides in clay-shales (CS), and rockslides in flysch rocks (FS).

Data Records

The MIRAGE dataset is composed of the three following products, all provided in the WGS 84 / UTM zone 32N (EPSG:32632) coordinate system:

1. Wrapped interferograms in TIFF format, with a pixel resolution of 15 m.
2. Coherence maps in TIFF format, one for each corresponding interferogram, with a pixel resolution of 15 m.

3. Labels in shapefile format, one for each corresponding interferogram. Each shapefile contains the following seven attributes:
    - *Id*: the numeric unique identifier, ranging from “1” to n polygons.
    - *Class*: the mass movement type assigned to the interferometric signal, indicated by its initial (e.g. “RS” as rockslide, etc).
    - *Sign_Qual*: the quality of the interferometric signal (i.e. “1” as high or “2” as low).
    - *Class_Unc*: the uncertainty of the assigned mass movement type classification for the interferometric signal (i.e. “1” as low or “2” as high).
    - *IFG*: the acquisition dates of the image pair used to generate the interferogram, written as “master_slave” in the yy/mm/dd format (e.g. “20190816_20190822”)
    - *Bt*: temporal baseline of the interferogram, written in days format (e.g. “6”, “365”, etc).
    - *Traj*: trajectory or orbit of the images used for the interferogram (i.e. “A” as ascending or “D” as descending).

A total of 92 interferograms are provided for the analysed areas, with 36 for the Central Alps and 56 for the Northern Apennines. The selected interferograms show an average coherence of 0.45, with only around 15 % of pixels below 0.2, which is considered acceptable given the challenging terrain, including abundant vegetation in the Northern Apennines and steep, seasonally snow-covered slopes in the Central Alps. While summer is the optimal season for more coherent interferograms in the Central Alps due to snow-free conditions, it is the least suitable in the Northern Apennines as vegetation growth causes strong decorrelation, making winter to spring the most favourable period instead.

The dataset includes 4910 labels, with 2667 for the Central Alps and 2243 for the Northern Apennines (Table 2). A high degree of overlap among labels within both areas indicates that most correspond to repeated detections of the same mass movements, captured across different interferograms. This implies that a total of 550 individual mass movement processes were captured in the Central Alps and 233 in the Northern Apennines. In the Central Alps, rock glaciers represent the dominant mass movement class (RG; 65.9%), that together with talus (TA; 8.4%) and protalus rampart (PR; 6.3%), evidence the strong periglacial influence on slope dynamics in this area (Table 2). Deep-seated landslides (DG) and rockslides (RS) accounts for approximately 6-7% each, while debris slides (DS) represent only 3.3% (Table 2). In the Apennines, most labels correspond to earthflows (CF; 50.5 %), followed by earthslides involving clay-shales (CS; 29%) and rockslides in flysch rocks (FS; 7.8%) (Table 2), reflecting the dominance of slow-moving clay-rich and lithological-controlled failures in this region. A representative number of artifacts (AR) related to geometrical distortions or atmospherics patches were also mapped for each study area, with 284 labels in the Northern Apennines and 80 in the Central Alps. Notably, we intentionally included artifacts that resemble real displacement signals but lack geomorphological consistency, because they were particularly

prone to misinterpretation. Excluding the artifacts, our labels dataset results in 4546 labels corresponding to active mass movements signals.

Mass movement class	Nº labels	% of total labels	Mean area (km^2)	Main baseline (days)	Phase signal pattern (shape, texture)
Artifact (AR)	80	3.0	0.11	-	-
Deep-seated deformation (DG)	157	5.9	0.65	365	Broad, homogeneous
Debris slide (DS)	89	3.3	0.10	365	Localised, heterogeneous
Protalus rampart (PR)	168	6.3	0.04	12	Elongated, heterogeneous
Rock glacier (RG)	1757	65.9	0.04	12	Elongated, homogeneous
Rockslide (RS)	192	7.2	0.13	365	Localised, homogeneous
Talus (TA)	224	8.4	0.05	12	Elongated, heterogeneous
Total Central Alps	**2667**				
Artifact (AR)	284	12.7	0.08	-	-
Earthflow in clay-shales (CF)	1132	50.5	0.06	12	Elongated, homogeneous
Earthslide in clay-shales (CS)	651	29.0	0.06	12	Localised, homogeneous
Rockslide in flysch rocks (FS)	176	7.8	0.07	12	Localised, homogeneous
Total Northern Apennines	**2243**				

Table 2. Labels class distribution and their main characteristics.

Regarding the acquisition geometry, labels from the Central Alps are predominantly from descending track interferograms (60%), whereas ascending tracks prevail in the Northern Apennines (75%). Regarding the temporal baselines, generating interferograms over a wide range of temporal baselines (Bt) was crucial to capture signals representative of different mass movement classes and to assess their typical timescales of occurrence. In the Central Alps, 1-year baseline allows to detect most deep-seated landslides (DG, DS and RS) (Fig. 3). Debris slides (DS) and rockslides (RS) are also captured at shorter baselines, although their detection progressively increase towards longer baseline. The most frequent baseline for periglacial landforms (RG, PR, and TA) is 12-days, although longer baselines also perform well, particularly for rock glaciers (RG), indicating their higher heterogeneous kinematics. For the Northern Apennines, 12 days baseline shows the higher peak for the three landslide types (DF, CS and FS) in terms of the total number of detected signals (Fig. 3), which is mainly influenced by the greater number of labelled 12-day interferograms. Based on our observations, however, all the investigated temporal baselines from 6 to 24 days demonstrated comparable performance for the detection of active landslides in this area. The 30-days baseline only occasionally allowed a solid interpretation given both the low reliability of the phase information and the high noise levels.

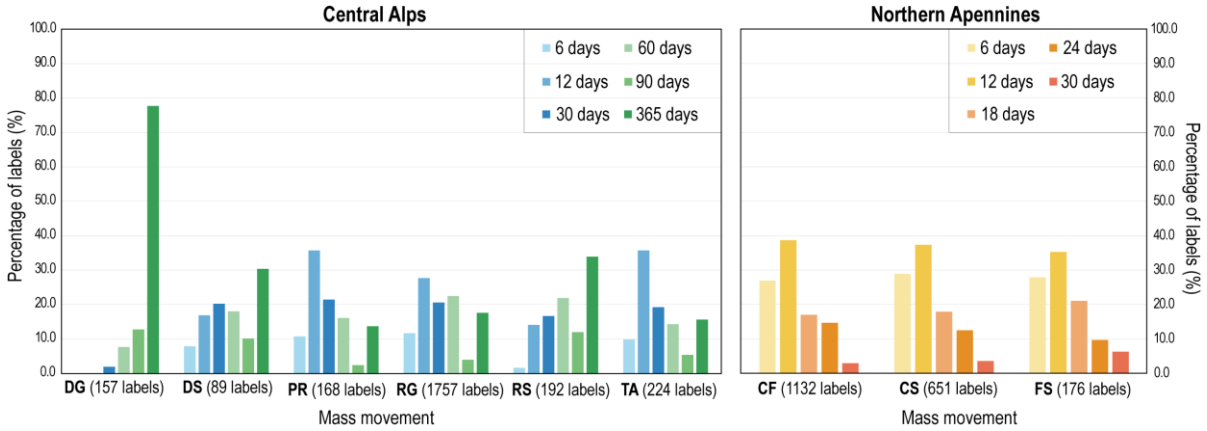

Figure 3. Distribution of labels in the Central Alps and Northern Apennines showed as the relative percentages of labels per baseline within each mas movement (DG: deep-seated gravitational slope deformation, DS: debris slide, PR: protalus rampart, RG: rock glacier, RS: rockslide, TA: talus, CF: earthflows in clay-shales, CS: earthslides in shales/marls, FS: rockslides in flysch rocks).

Data Overview

The interferometric wrapped phase signals can exhibit diverse patterns among different types of mass movements. While these patterns are not universal, certain shape and texture characteristics were observed more frequently for specific movement types in our dataset (Table 2). The shape describes the external geometry of the signal, and we identified three main shape patterns: (1) broad, that correspond to considerably wide areas affected by the movements; (2) localised, that is limited to smaller and specific areas, often with sharper phase gradients at the boundaries; and (3) elongated, that are patterns stretched along a preferential direction, typically reflecting a channelised or creeping displacement. The texture describes the internal organisation of the phase signal, and we observed two main types: (1) homogeneous, that reflects a coherent and relatively uniform phase pattern over the movement area; and (2) heterogeneous, that shows variations in the phase continuity as an irregular or fragmented movement.

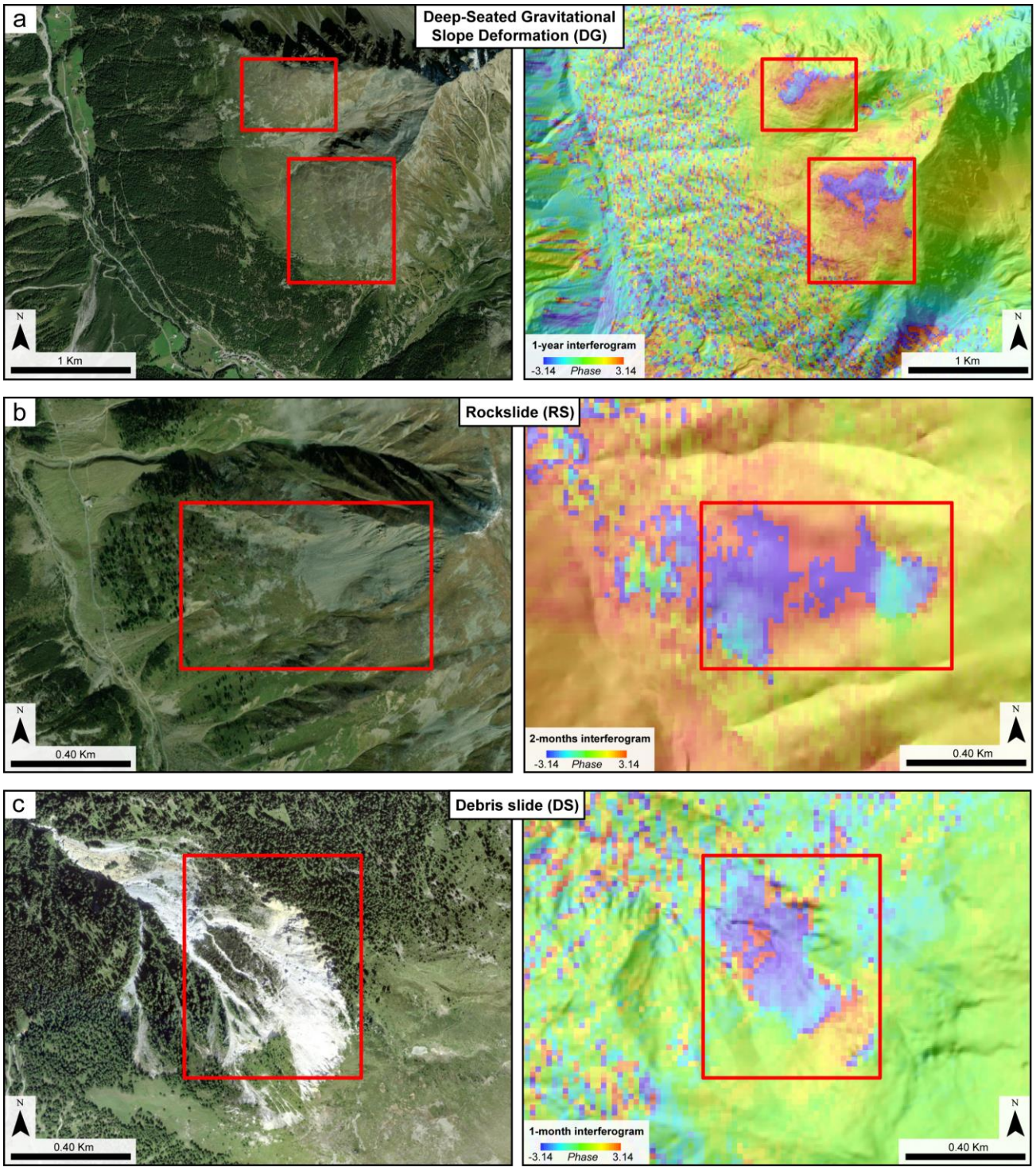

Figure 4. Examples of labels in the Central Alps study area: **(a)** deep-seated gravitational slope deformation (DG), **(b)** rockslide (RS), and **(c)** debris slide (DS). The bounding box is indicated by the red rectangle.

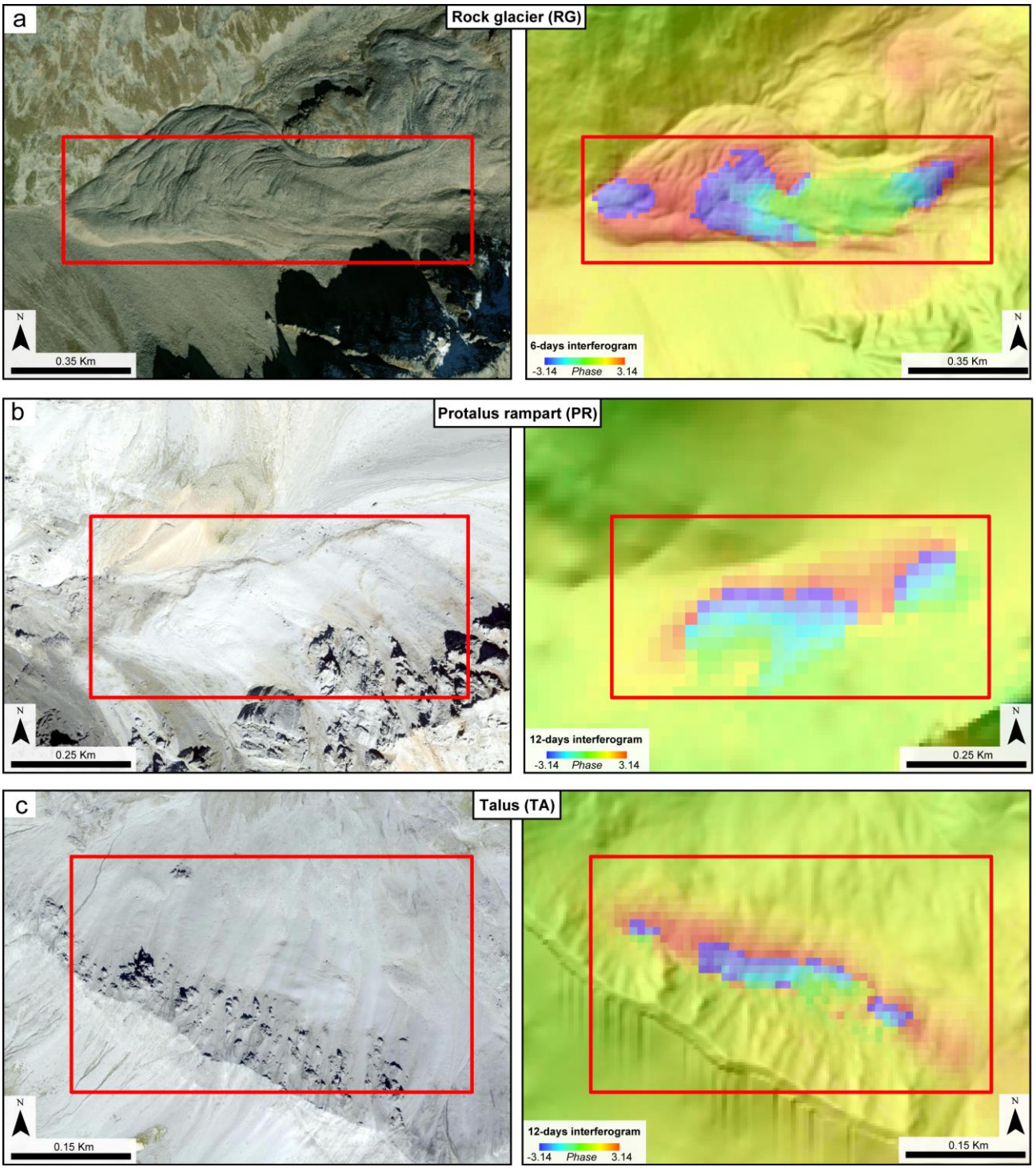

Figure 5. Examples of labels in the Central Alps study area: **(a)** rock glacier (RG), **(b)** protalus rampart (PR), and **(c)** talus (TA). The bounding box is indicated by the red rectangle.

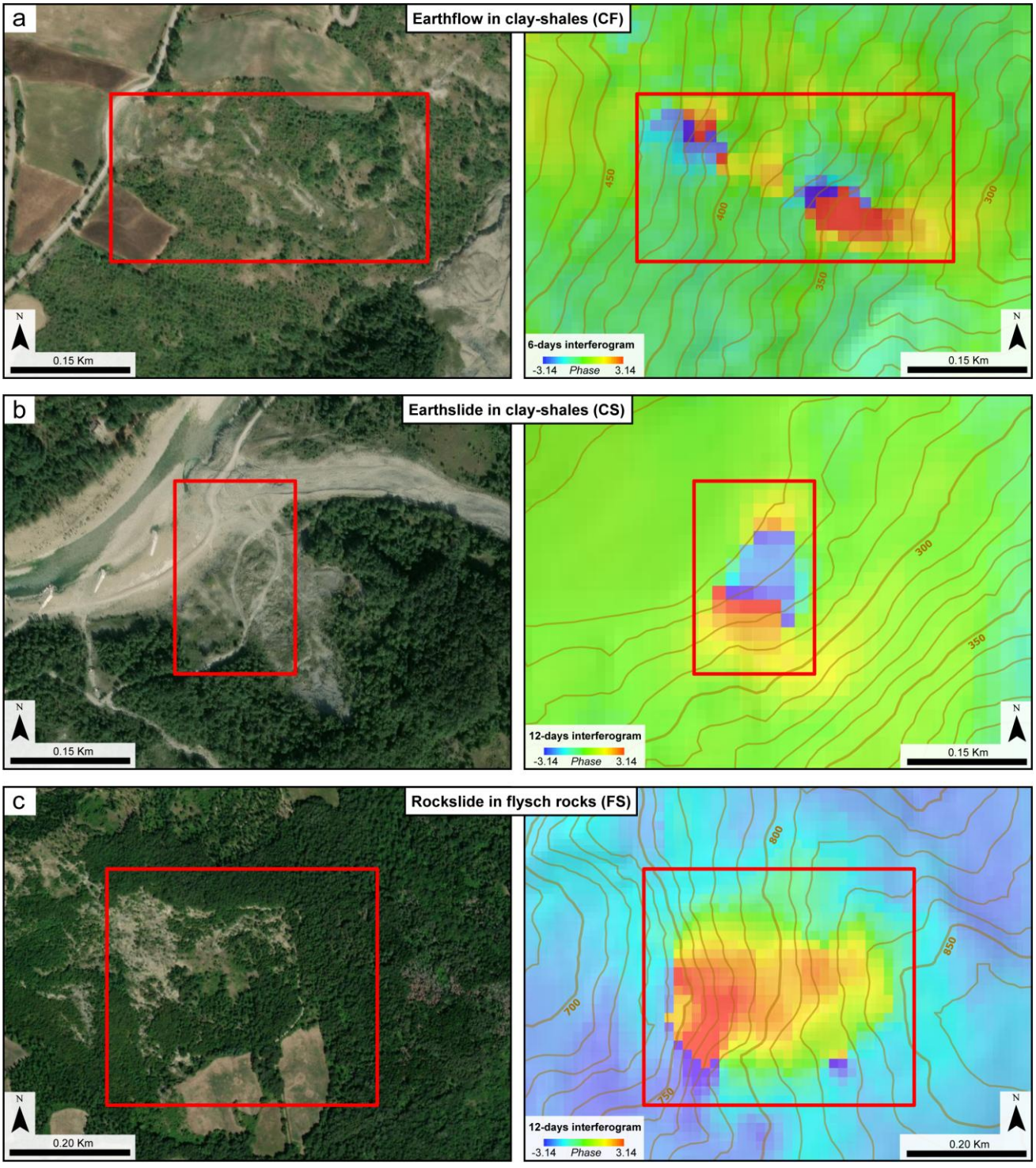

Figure 6. Examples of labels in the Northern Apennines study area: **(a)** earthflow in clay-shales (CF), **(b)** earthslide in clay-shales (CS), and **(c)** rockslide in clay-shales (FS). The bounding box is indicated by the red rectangle.

In the Central Alps area, deep-seated gravitational slope deformations (DG) show broad and homogeneous signal patterns, generally covering a continuous and extensive areas of the slope (Fig. 4a). In contrast, rockslides (RS) and debris slides (DS) both exhibit localised signal patterns concentrated within the landslide body (Fig. 4b, 4c), but rockslides display a homogeneous pattern consistent with block-like movement, whereas debris slides show a heterogeneous pattern resulting from the movement of the fragmented material. Rock glaciers (RG) display elongated and generally homogeneous signal patterns, being well-aligned with their characteristic wrinkled morphology and their slow creeping movement (Fig. 5a). Protalus ramparts (PR) and talus (TA) also exhibit elongated signals, but these are more heterogenous, suggesting diffuse debris mobilisation at the slope foot and more limited creeping than rock glaciers (Fig. 5b, 5c). In the Northern Apennines area, the interferometric signals of the three landslide types commonly display similar homogeneous patterns that extend from the perimeter toward the centre of the landslide body area, attributed to a viscous-type movement of the fine-grained weak rocks involved (Fig. 6). Earthslides (CS) and rockslides (RS) both exhibit a localised signal shape, typically with roughly equal length and width, and generally steep phase gradients at the landslide boundaries (Fig. 6a, 6b). Contrarily, earthflows (CF) commonly exhibit downslope-elongated signals, reflecting the channelised flow direction, with higher phase gradients perpendicular to the direction of movement (Fig. 6a).

Technical Validation

We addressed the geomorphological consistency of the mapped signal dataset by evaluating: (1) the frequency distributions of key morphometric variables inside and outside the labels; and (2) the non-cumulative frequency-area distributions of the labels compared to the typical one of the corresponding mass movements, as evaluated in the literature. These analyses were performed to validate the geomorphological significance of the mapped signals and their consistency with the real phenomena represented in the dataset.

Frequency distribution of geomorphological variables in labels

We extracted the frequency distribution of relevant morphometric variables such as aspect, curvature, convexity, slope, Terrain Ruggedness Index (TRI) and Topographic Wetness Index (TWI), both inside the labels and outside (i.e. stable areas). For each class, we compared the distribution of pixel values within the labels (“inside”) with an equal number of randomly sampled pixel values from non-affected areas (“outside”). This type of analysis can support the use of morphometric variables as diagnostic tools to infer underlying geomorphological geological processes during the labelling process. Moreover, this comparison can highlight a geomorphological significance of the detected displacement signals. Figure 7 shows the histograms of two of these variables, slope and TRI, for the two main classes of the Central Alps (DG and RG) and the main class of the Northern Apennines (CF).

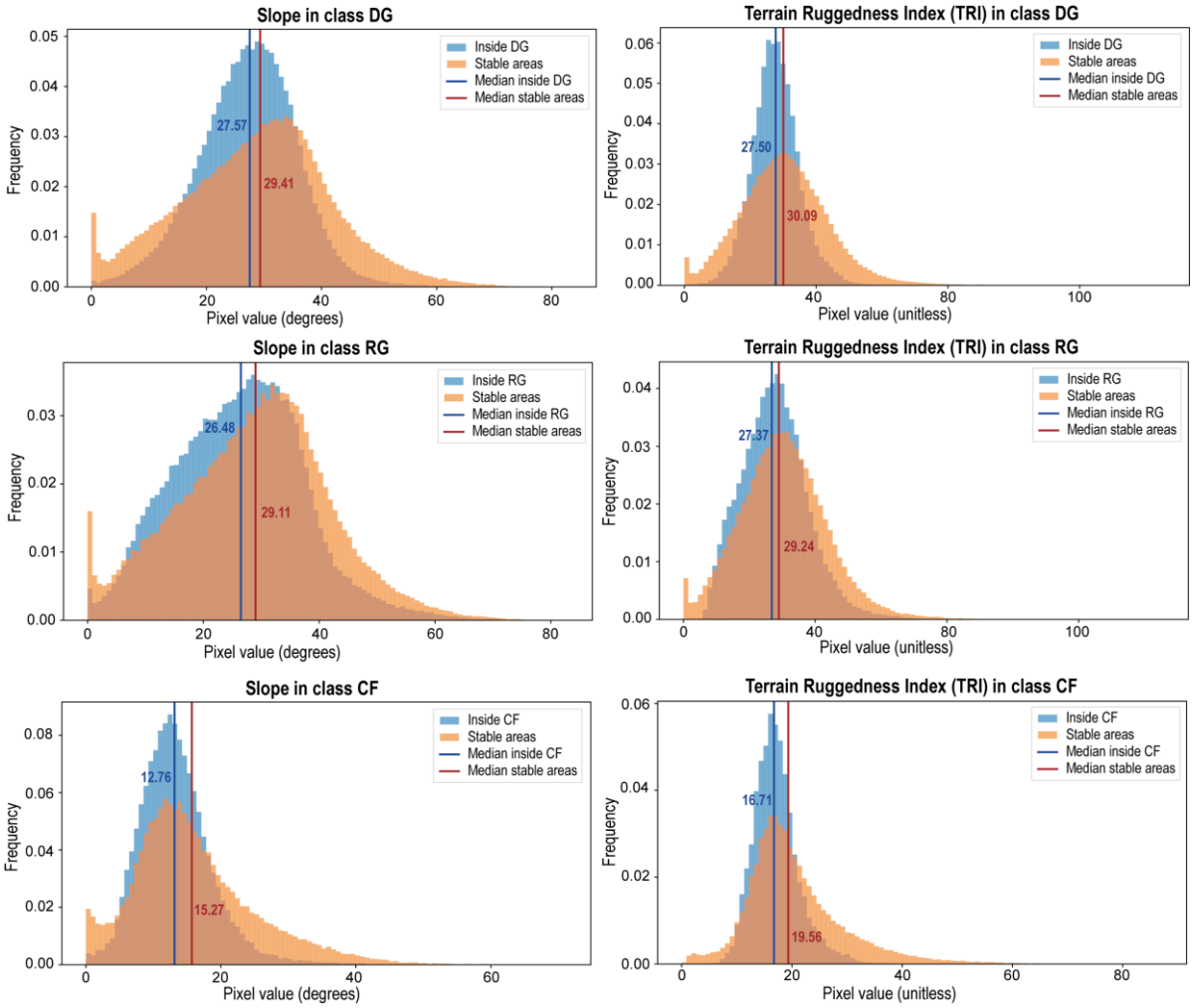

Figure 7. Histograms of slope and Terrain Ruggedness Index (TRI) computed for areas inside and outside the labels for the main mass movement types in the Central Alps (DG: deep-seated gravitational slope deformation, RG: rock glacier) and the Northern Apennines (CF: earthflow in clay-shales).

Overall, the mass movements in the Alps have been developed in a high local relief range with steep slopes (e.g. 26-27º in DG and RG), while landslides in the Apennines are mainly controlled by the stratigraphic characteristics of weak lithologies and affect subdued slopes (e.g. around 13º in CF) (Figure 7). The difference of 2-3º between inside and outside labels for the alpine classes (DG and RG) are not so relevant, meaning that slope is not a very discriminant variable of active mass movements in this area. This agrees with the TRI distributions, which show only subtle contrasts between stable and unstable areas in both DG and RG, as in these alpine settings, the overall roughness is already high due to the typical rocky terrain and strong relief. For instance, deep-seated slope deformations (DG) are controlled mainly by structural conditions rather than by local steepness or surface

roughness, while rock glaciers (RG) are more influenced by permafrost dynamics than by either slope or TRI alone. However, even if the median values do not show a highly significant difference, the shape of the histograms reveals variations between areas within and outside the labels (Fig. 7). Specifically, the distributions within the labels (i.e., active movements) approximate a normal distribution, whereas stable areas show more asymmetric distributions with a long tail towards higher values, suggesting a more defined geomorphological context for the active processes.

Contrarily in the Apennines, landslides in clay-rich materials (e.g. earthflows) display a more significant difference of slope between unstable (inside the labels) and stable areas (~6º), highlighting a higher relevance of the local steepness. This pattern is mirrored by TRI values, which show a clearer distinction between active earthflows and surrounding stable slopes. The lower background roughness of the Apennines and the weak mechanical resistance of the involved lithologies allow the deformation to generate a recognisable TRI signal, even though general TRI values remain lower than in the Alps. Steeper slopes are usually covered by dense vegetation and remain stable, while gentler and smoother reliefs (e.g. cultivated fields) often host incipient instability processes that may evolve into fully developed failures, leading to localised increases in surface roughness. As observed in the Alps, the shapes of the histograms also differ, with areas within the labels approximating a normal distribution, while stable areas exhibit an asymmetric distribution with a long tail towards higher values (Fig. 7).

Non-cumulative frequency-area distribution in labels

The magnitude-frequency analysis of the areas mapped by our bounding boxes was carried out through a power law fitting. This relationship can serve as a key indicator of the underlying mass movement process and increase the reliability of the mapping. In our study area in the Alps, the exponent β ranges from 2 to 3 for the three landslide types (DG, DS, and RS) (Fig. 8). Interestingly, although the values are not directly comparable with those referring to landslide areas inventoried as polygons, they still fall within the same general range (e.g. Van Den Eeckhaut et al., 2007 and references therein, Agliardi et al., 2013; Crosta et al., 2013; Frattini and Crosta, 2013). Moreover, the overall shape of the distribution is preserved, indicating that the bounding-box mapping retains the scaling behaviour of the phenomena.

In the analysed area of the Northern Apennines, β values around 3 represent a good fit for both slide types (FS and CS) (e.g. (Guzzetti et al., 2002; Malamud et al., 2004), whereas for earthflows (CF) the exponent is significantly higher (Fig. 8). This difference can reasonably be attributed to the abundance of small-area labels in this class, which correspond only to active portions of the entire deposit, usually confined to the source zone where the main deposit forms through the downslope coalescence of smaller phenomena. Regarding the periglacial landforms, frequency-area analyses are rarely performed and not suitable for comparison.

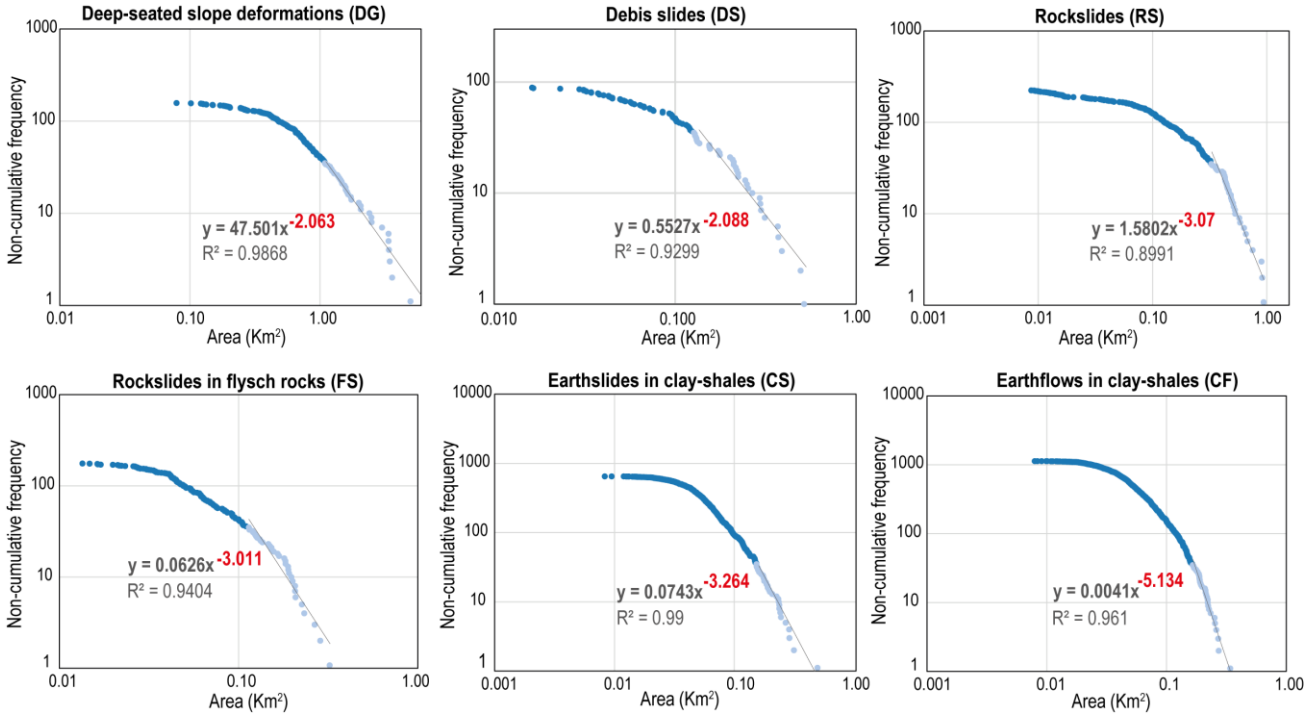

Figure 8. Analysis of non-cumulate frequency-area of the landslide classes in the Alps (DG, DS, RS) and the Apennines (FS, CS, CF), computed for areas inside the labels of each type. The value β (highlighted in red) corresponds to the exponent of the power-law fitting for each mass movement type.

Usage Notes

We encourage the use of the MIRAGE dataset for training and validating deep learning models (e.g., convolutional object detectors such as YOLO; Mondini et al., 2025) for the automated detection and classification of mass movements. It is important to remark that the dataset includes a variety of displacement signal patterns associated with very different types of mass movements and geomorphological settings. We distinguished nine types of mass movements: six landslide types and three related to periglacial movements. Moreover, the dataset integrates movements across two different geological and geomorphological contexts: an alpine landscape shaped by past glacial activity with hard metamorphic lithologies (Central Alps) and a gentle landscape shaped by fluvial activity with weak fine-grained lithologies (Northern Apennines). This is expected to improve the robustness and transferability of AI-based models designed for interferometric signal interpretation. Users should consider that the displacement signals were extracted from interferograms generated using a variable range of temporal baselines, reflecting the highly heterogeneous temporal behaviour of mass movements, from very slow to relatively faster

processes. Consequently, some signal patterns may be more clearly visible under specific temporal configurations, and this variability should be taken into account when using the dataset for model development.

We also encourage users aiming to extend the MIRAGE dataset or generate similar datasets in other regions to adopt labelling strategies comparable to those proposed in the workflow of this dataset, in order to minimise the risk of misinterpreting interferometric artefacts as real displacement signals. It is important to note that the interpretation of wrapped interferograms is intrinsically challenging due to the presence of noise, atmospheric artefacts and the often subtle nature of displacement signals. For this reason, the labelling of datasets of this type should rely strongly on geomorphological expertise and on the integration of ancillary datasets, including landslide inventories, topographic data, orthophotos and aerial imagery. To facilitate signal interpretation, we describe some common geometries (e.g., broad, localised or elongated) and textural characteristics (e.g., homogeneous or heterogeneous) that may assist in distinguishing between different processes, both within the present dataset and in other datasets. These descriptions are expected to support manual interpretation as well as the development of automated detection strategies.

Data availability

The MIRAGE dataset, composed of wrapped interferograms, coherence maps and labels, is freely available via Zenodo at https://doi.org/10.5281/zenodo.17899662 (Reyes-Carmona et al., 2025).

Author contributions

FA, AMo and AS conceived the research and designed the methodology. CRC and AMe performed DInSAR processing and signal mapping. CRC, AMe, FA and AS analysed and validated the results. CRC and AMe wrote the paper. FA, AMo, AS and FB revised and contributed to the paper. FA, AM and AS managed the project.

Funding

This research was funded by the European Union - Next Generation EU, Mission 4, Component 2, CUP H53D23001660006 (PRIN22 Project "MIRAGE: Mass movement Investigation and prediction through geomorphology, Remote sensing and Artificial intelligence"), and partially supported by the Italian Ministry of University and Research (MUR) project “Dipartimenti di Eccellenza 2023-2027, Department of Earth and Environmental Sciences, University of Milano-Bicocca". English language editing and style improvements were assisted using the AI tool ChatGPT (OpenAI, 2023).

Competing Interests

The authors declare that they have no conflict of interest.

References

Agliardi, F., Crosta, G. B., Frattini, P. & Malusà, M. G. Giant non-catastrophic landslides and the long-term exhumation of the European Alps. Earth Planet. Sci. Lett. 365, 263-274, (2013). https://doi.org/10.1016/j.epsl.2013.01.030 (2013).

Agliardi, F., Scuderi, M. M., Fusi, N. & Collettini, C. Slow-to-fast transition of giant creeping rockslides modulated by undrained loading in basal shear zones. Nat. Commun. 11, 1352, https://doi.org/10.1038/s41467-020-15093-3 (2020).

Agliardi, F. & Crippa, C. Deep-seated gravitational slope deformations, Treatise on Geomorphology, Second Edition, Elsevier, 183-199, https://doi.org/10.1016/B978-0-12-818234-5.00182-6 (2022).

Agliardi, F., Crippa, C., Codara, D. & Franzosi, F. Rapid regional assessment of rock glacier activity based on DInSAR wrapped-phase signal, The Cryosphere 19, 5003-5021. https://doi.org/10.5194/tc-19-5003-2025, (2025).

Anantrasirichai, N., Biggs, J., Albino, F., Hill, P. & Bull, D. Application of machine learning to classification of volcanic deformation in routinely generated InSAR data, J. Geophys. Res. Solid Earth 123, 6592-6606, https://doi.org/10.1029/2018JB015911 (2018).

Anantrasirichai, N., Biggs, J., Albino, F. & Bull, D. The application of convolutional neural networks to detect slow, sustained deformation in InSAR time series. Geophys. Res. Lett. 46, 11850-11858, https://doi.org/10.1029/2019GL084993 (2019).

Bayer, B., Simoni, A., Schmidt, D. & Bertello, L. Using advanced InSAR techniques to monitor landslide deformations induced by tunneling in the Northern Apennines, Italy. Eng. Geol. 226, 20-32, https://doi.org/10.1016/j.enggeo.2017.03.026 (2017).

Berardino, P., Fornaro, G., Lanari, R. & Sansosti, E. A new algorithm for surface deformation monitoring based on small baseline differential SAR interferograms. IEEE Trans. Geosci. Remote Sens. 40, 2375-2383, https://doi.org/10.1109/TGRS.2002.803792 (2003).

Bertello, L., Berti, M., Castellaro, S. & Squarzoni, G. Dynamics of an active earthflow inferred from surface wave monitoring. J. Geophys. Res. Earth Surf. 123, 1811-1834, https://doi.org/10.1029/2017JF004233 (2018).

Berti, M., Bertello, L., Bernardi, A. R., & Caputo, G. Back analysis of a large landslide in a flysch rock mass, Landslides 14, 2041-2058, https://doi.org/10.1007/s10346-017-0852-5 (2017).

Boeckli, L., Brenning, A., Gruber, S. & Noetzli, J. Permafrost distribution in the European Alps: calculation and evaluation of an index map and summary statistics, The Cryosphere 6, 807-820, https://doi.org/10.5194/tc-6-807-2012 (2012).

Borgatti, L., Corsini, A., Barbieri, M., Sartini, G., Truffelli, G., Caputo, G. & Puglisi, C. Large reactivated landslides in weak rock masses: a case study from the Northern Apennines (Italy). Landslides 3, 115-124, https://doi.org/10.1007/s10346-005-0033-9 (2006).

Bountos, N. I., Papoutsis, I., Michail, D., Karavias, A., Elias, P. & Parcharidis, I. Hephaestus: A large scale multitask dataset towards InSAR understanding, IEEE/CVF Proceedings 1453-1462, (2022).

Bralet, A., Trouvé, E., Chanussot, J. & Atto, A. M. ISSLIDE: A new InSAR dataset for Slow SLIding area DEtection with machine learning. IEEE Geosci. Remote Sens. Lett. 21, 1-5, https://doi.org/10.1109/LGRS.2024.3365299 (2024).

Brardinoni, F., Vivero, S., Barboux, C., Bodin, X., Cicoira, A., Echelard, T., Hu, Y., Jones, N., Lambiel, C., MacDonell, S., Pellet, C., Rouyet, L.; Ruiz, L., Schaffer, N., Wehbe, M. & Delaloye, R. RGIK guidelines for compiling consistent rock glacier inventories, Geomorphology 492, 110050, https://doi.org/10.1016/j.geomorph.2025.110050 (2026).

Brengman, C. M. & Barnhart, W. D. Identification of surface deformation in InSAR using machine learning. Geochem. Geophys. Geosyst. 22, e2020GC009204, https://doi.org/10.1029/2020GC009204 (2021).

Casagli, N., Intrieri, E., Tofani, V., Gigli, G. & Raspini, F. Landslide detection, monitoring and prediction with remote-sensing techniques, Nat. Rev. Earth Environ. 4, 51-64, https://doi.org/10.1038/s43017-022-00373-x (2023).

Cicoira, A., Marcer, M., Gärtner-Roer, I., Bodin, X., Arenson, L. U. & Vieli, A. A general theory of rock glacier creep based on in-situ and remote sensing observations. Permafr. Periglac. Process. 32, 139-153, https://doi.org/10.1002/ppp.2090 (2021).

Conti, P., Manatschal, G. & Pfister, M. Synrift sedimentation, Jurassic and Alpine tectonics in the central Ortler nappe (Eastern Alps, Italy). Eclogae. Geol. Helv. 87, 63-90, (1994).

Corsini, A., Farina, P., Antonello, G., Barbieri, M., Casagli, N., Coren, F., Guerri, L., Ronchetti, F., Sternai, P. & Tarchi, D. Space-borne and ground-based SAR interferometry as tools for landslide hazard management in civil protection, Int. J. Remote Sens. 27, 2351-2369, https://doi.org/10.1080/01431160600554405 (2006).

Coulson, A. V., Thomas, W. H. & Wang, C. A Comparative Study of Deep Learning-Based Models for Object Detection in Remote Sensing Imagery, Int. Arch. Photogramm. Remote Sens. Spatial Inf. Sci. XLVIII-M-5-2024, 201-205, https://doi.org/10.5194/isprs-archives-XLVIII-M-5-2024-201-2025 (2025).

Crippa, C., Franzosi, F., Zonca, M., Manconi, A., Crosta, G. B., Dei Cas, L. & Agliardi, F. Unraveling spatial and temporal heterogeneities of very slow rock-slope deformations with targeted DInSAR analyses. Remote Sens. 12, 1329, https://doi.org/10.3390/rs12081329 (2020).

Crippa, C., Valbuzzi, E., Frattini, P., Crosta, G. B., Spreafico, M. C. & Agliardi, F. Semi-automated regional classification of the style of activity of slow rock-slope deformations using PS InSAR and SqueeSAR velocity data, Landslides 18, 2445-2463, https://doi.org/10.1007/s10346-021-01654-0 (2021).

Crippa, C., Steger, S., Cuozzo, G., Bearzot, F., Mair, V. & Notarnicola, C. Optimizing rock glacier activity classification in South Tyrol (northeastern Italy): integrating multisource data with statistical modelling, The Cryosphere 19, 3493-3515. https://doi.org/10.5194/tc-19-3493-2025 (2025).

Crosta, G. B. & Agliardi, F. Failure forecast for large rock slides by surface displacement measurements, Can. Geotech. J. 40, 176-191, https://doi.org/10.1139/t02-085 (2003).

Crosta, G. B., Chen, H. & Lee, C. F. Replay of the 1987 Val Pola landslide, Italian alps, Geomorphology 60, 127-146, https://doi.org/10.1016/j.geomorph.2003.07.015 (2004).

Crosta, G. B., Frattini, P. & Agliardi, F. Deep seated gravitational slope deformations in the European Alps. Tectonophysics 605, 13-33, https://doi.org/10.1016/j.tecto.2013.04.028 (2013).

Crosta, G. B., Agliardi, F., Rivolta, C., Alberti, S. & Dei Cas, L. Long-term evolution and early warning strategies for complex rockslides by real-time monitoring. Landslides 14, 1615-1632, https://doi.org/10.1007/s10346-017-0817-8 (2017).

Dini, B., Manconi, A. & Loew, S. Investigation of slope instabilities in NW Bhutan as derived from systematic DInSAR analyses, Eng. Geol. 259, 105111, https://doi.org/10.1016/j.enggeo.2019.04.008 (2019).

Fadhillah, M. F., Hakim, W. L., Park, S., Kim, D., Park, Y. C., Kim, C. H. & Lee, C. W. Surface deformation simulation for InSAR detection using a machine learning approach on the hantangang river volcanic field: A case study on the orisan mountain. Front. Environ. Sci. 10, 968120, https://doi.org/10.3389/fenvs.2022.968120 (2022).

Fattahi, H. & Amelung, F. InSAR bias and uncertainty due to the systematic and stochastic tropospheric delay, J. Geophys. Res. Solid Earth 120, 8758-8773, https://doi.org/10.1002/2015JB012419 (2015).

Ferretti, A., Prati, C. and Rocca, F. Permanent scatterers in SAR interferometry, IEEE Trans. Geosci. Remote Sens. 39, 8-20, https://doi.org/10.1109/36.898661 (2002).

Fey, C. & Krainer, K. Analyses of UAV and GNSS based flow velocity variations of the rock glacier Lazaun (Ötztal Alps, South Tyrol, Italy). Geomorphology 365, 107261, https://doi.org/10.1016/j.geomorph.2020.107261 (2020).

Frattini, P. & Crosta, G. B. The role of material properties and landscape morphology on landslide size distributions, Earth Planet. Sci. Lett. 361, 310-319, https://doi.org/10.1016/j.epsl.2012.10.029 (2013).

Froitzheim, N., Schmid, S. & Conti, P. Repeated change from crustal shortening to orogen-parallel extension in the Austroalpine units of Graub" unden. Eclogae. Geol. Helv. 87, 559-612 (1994).

Froitzheim, N. & Manatschal, G. Kinematics of Jurassic rifting, mantle exhumation, and passive-margin formation in the Austroalpine and Penninic nappes (eastern Switzerland). Geol. Soc. Am. Bull., 108, 1120-1133, https://doi.org/10.1130/0016-7606(1996)108<1120:KOJRME>2.3.CO;2, 1996.

Fu, L., Zhang, Q., Wang, T., Li, W., Xu, Q. & Ge, D. Detecting slow-moving landslides using InSAR phase-gradient stacking and deep-learning network. Front. Environ. Sci. 10, 963322, https://doi.org/10.3389/fenvs.2022.963322 (2022).

Goldstein, R. M. & Werner, C. L. Radar interferogram filtering for geophysical applicationsm, Geophys. Res. Lett. 25, 4035-4038 (1998).

Grämiger, L. M., Moore, J. R., Gischig, V. S., Ivy-Ochs, S. & Loew, S. Beyond debuttressing: Mechanics of paraglacial rock slope damage during repeat glacial cycles, J. Geophys. Res. Earth Surf. 122, 1004-1036, https://doi.org/10.1002/2016JF003967 (2017).

Gui, S., Song, S., Qin, R. & Tang, Y. Remote sensing object detection in the deep learning era - a review. Remote Sens. 16, 327. https://doi.org/10.3390/rs16020327 (2024).

Guzzetti, F., Malamud, B. D., Turcotte, D. L. & Reichenbach, P. Power-law correlations of landslide areas in central Italy. Earth Planet. Sci. Lett. 195, 169-183, https://doi.org/10.1016/S0012-821X(01)00589-1 (2002).

Guzzetti, F., Mondini, A. C., Cardinali, M., Fiorucci, F., Santangelo, M. & Chang, K. T. Landslide inventory maps: New tools for an old problem, Earth-Sci. Rev. 112, 42-66, https://doi.org/10.1016/j.earscirev.2012.02.001 (2012).

He, K., Zhang, X., Li, Z., Jiang, W., Zhou, J. & Han, B. A mask r-cnn network for wide-area mining subsidence automatic detection with insar observations, IEEE Geosci. Remote Sens. 62, 1-16, https://doi.org/10.1109/TGRS.2024.3360968 (2024).

Hooper, A., Gaddes, M., Bagnardi, M. & Albino, F. Towards improved forecasting of volcanic hazards using machine learning applied to InSAR data, 2021 IGARSS, 8484-8486), https://doi.org/10.1109/IGARSS47720.2021.9555049 (2021).

Korup, O., Densmore, A. L. & Schlunegger, F. The role of landslides in mountain range evolution, Geomorphology, 120, 77-90, https://doi.org/10.1016/j.geomorph.2009.09.017 (2010).

IFFI - Inventario dei Fenomeni Franosi in Italia (Landslide Inventory of Italy), Istituto Superiore per la Protezione e la Ricerca Ambientale (ISPRA). https://www.isprambiente.gov.it/it (2017).

INSPIRE Geoportal - Catasto dei Rock Glacier in Alto Adige. https://inspire-geoportal.ec.europa.eu/srv/api/records/p_bz:Geology:RockGlaciers?language=all (2010).

Li, Z., Wang, Y., Zhang, N., Zhang, Y., Zhao, Z., Xu, D., Ben, G. & Gao, Y. Deep learning-based object detection techniques for remote sensing images: A survey. Remote Sens. 14, 2385. https://doi.org/10.3390/rs14102385 (2022).

Liu, X., Wang, Z., Zhang, Y., Shan, X. & Liu, Z. A Global Coseismic InSAR Dataset for Deep Learning: Automated Construction from Sentinel-1 Observations (2015-2024). Remote Sens. 17, 1832, https://doi.org/10.3390/rs17111832 (2025).

Malamud, B. D., Turcotte, D. L., Guzzetti, F. & Reichenbach, P. Landslide inventories and their statistical properties, Earth Surf. Process. Landf. 29, 687-711, https://doi.org/10.1002/esp.1064 (2004).

Manconi, A. How phase aliasing limits systematic space-borne DInSAR monitoring and failure forecast of alpine landslides. Eng. Geol. 287, 106094, https://doi.org/10.1016/j.enggeo.2021.106094 (2021).

Mondini, A. C., Guzzetti, F., Chang, K. T., Monserrat, O., Martha, T. R. & Manconi, A. Landslide failures detection and mapping using Synthetic Aperture Radar: Past, present and future, Earth-Sci. Rev. 216, 103574, https://doi.org/10.1016/j.earscirev.2021.103574 (2021).

Mondini, A., Bovenga, F., Simoni, A., Reyes-Carmona, C., Mercurio, A. & Agliardi F.: Automated detection of active mass movements in SAR interferograms using Deep Learning, EGU General Assembly Abstracts, https://doi.org/10.5194/egusphere-egu25-16692 (2025).

Pavan, V., Tomozeiu, R., Cacciamani, C. & Di Lorenzo, M. Daily precipitation observations over Emilia-Romagna: mean values and extremes. Int. J. Climatol. 28, 2065-2079, https://doi.org/10.1002/joc.1694 (2008).

Pini, G. A. Tectonosomes and olistostromes in the Argille Scagliose of the Northern Apennines, Italy, Geological Society of America, Special Paper 335, 1-64. https://doi.org/10.1130/SPE335 (1999).

RER - Regione Emilia-Romagna, Banca dati geologica, 1:10.000 - Frane, depositi di versante e depositi alluvionali - 10k, Geoportale Emilia-Romagna, https://geoportale.regione.emilia-romagna.it/ (2024).

Reyes-Carmona, C., Mercurio, A., Mondini, A., Bovenga, F., Simoni, A. & Agliardi, F. MIRAGE: a geomorphology-constrained dataset of DInSAR wrapped phase signals from active mass movements, Version v1, Zenodo (dataset), https://doi.org/10.5281/zenodo.17899662 (2025).

Ricci Lucchi, F. The Oligocene to Recent foreland basins of the northern Apennines, Foreland basins, Foreland Basins: An Introduction, Wiley, 103-139, https://doi.org/10.1002/9781444303810.ch6 (1986).

Riva, F., Agliardi, F., Amitrano, D. & Crosta, G. B. Damage-based time-dependent modeling of paraglacial to postglacial progressive failure of large rock slopes. J. Geophys. Res. Earth Surf. 123, 124-141, https://doi.org/10.1002/2017JF004423 (2018).

RGIK - Rock Glacier Inventories and Kinematics, Guidelines for inventorying rock glaciers, International Permafrost Association (IPA), https://www.rgik.org/ (2023).

Ronchetti, F., Borgatti, L., Cervi, F., Gorgoni, C., Piccinini, L., Vincenzi, V. & Corsini, A. Groundwater processes in a complex landslide, northern Apennines, Italy, Nat. Hazards Earth Syst. Sci. 9, 895-904, https://doi.org/10.5194/nhess-9-895-2009 (2009).

Rotter, P., and Muron, W.: Automatic detection of subsidence troughs in SAR interferograms based on convolutional neural networks. IEEE Geosci. Remote Sens. Lett, 18, 82-86, https://doi.org/10.1109/LGRS.2020.2966079, 2020,

Sandwell, D., Mellors, R., Tong, X., Wei, M. & Wessel, P. GMTSAR: An InSAR Processing System Based on Generic Mapping Tools, Scripps Institution of Oceanography Technical Report (2011).

Santangelo, M., Cardinali, M., Bucci, F., Fiorucci, F. & Mondini, A. C. Exploring event landslide mapping using Sentinel-1 SAR backscatter products, Geomorphology 397, 108021. https://doi.org/10.1016/j.geomorph.2021.108021 (2022).

Scotti, R., Brardinoni, F., Alberti, S., Frattini, P. & Crosta, G. B. A regional inventory of rock glaciers and protalus ramparts in the central Italian Alps, Geomorphology 186, 136-149, https://doi.org/10.1016/j.geomorph.2012.12.028 (2013).

Silva, B., Sousa, J. J., Lazecky, M. & Cunha, A. Deformation fringes detection in SAR interferograms using deep learning, Procedia Comput. Sci. 196, 151-158. https://doi.org/10.1016/j.procs.2021.11.084 (2022).

Simoni, A., Ponza, A., Picotti, V., Berti, M., and Dinelli, E.: Earthflow sediment production and Holocene sediment record in a large Apennine catchment. Geomorphology 188, 42-53, https://doi.org/10.1016/j.geomorph.2012.12.006 (2013).

Tomozeiu, R., Busuioc, A., Marletto, V., Zinoni, F. & Cacciamani, C. Detection of changes in the summer precipitation time series of the region Emilia-Romagna, Italy. Theor. Appl. Climatol. 67, 193-200, https://doi.org/10.1007/s007040070008 (2000).

Van Den Eeckhaut, M., Poesen, J., Govers, G., Verstraeten, G. & Demoulin, A.: Characteristics of the size distribution of recent and historical landslides in a populated hilly region, Earth Planet. Sci. Lett. 256, 588-603, https://doi.org/10.1016/j.epsl.2007.01.040 (2007).

Wasowski, J. & Bovenga, F. Investigating landslides and unstable slopes with satellite Multi Temporal Interferometry: Current issues and future perspectives, Eng. Geol. 174, 103-138, https://doi.org/10.1016/j.enggeo.2014.03.003 (2014).

Zangerl, C., Eberhardt, E. & Perzlmaier, S. Kinematic behaviour and velocity characteristics of a complex deep-seated crystalline rockslide system in relation to its interaction with a dam reservoir, Eng. Geol. 112, 53-67, https://doi.org/10.1016/j.enggeo.2010.01.001 (2010).

Zebker, H. A., Rosen, P. A. & Hensley, S. Atmospheric effects in interferometric synthetic aperture radar surface deformation and topographic maps, J. Geophys. Res. Solid Earth 102, 7547-7563, https://doi.org/10.1029/1998GL900033 (1997).

Zhang, X., Zhang, T., Wang, G., Zhu, P., Tang, X., Jia, X. & Jiao, L. Remote sensing object detection meets deep learning: A metareview of challenges and advances, IEEE Geosci. Remote. Sens. Mag. 11, 8-44. https://doi.org/10.1109/MGRS.2023.3312347 (2023).

Zhang, R., Zhu, W., Fan, B., He, Q., Zhan, J., Wang, C. & Zhang, B.: MB-Net: A network for accurately identifying creeping landslides from wrapped interferograms, Int. J. Appl. Earth Obs. Geoinf. 135, 104300, https://doi.org/10.1016/j.jag.2024.104300 (2024).

Zhu, X. X., Montazeri, S., Ali, M., Hua, Y., Wang, Y., Mou, L., Shi, Y., Xu, F. & Bamler, R.: Deep learning meets SAR: Concepts, models, pitfalls, and perspectives, IEEE Geosci. Remote Sens. Mag. 9, 143-172, https://doi.org/10.1109/MGRS.2020.3046356 (2021).

Zhu, C., Li, X., Wang, C., Zhang, B. & Li, B.: Deep learning-based coseismic deformation estimation from InSAR interferograms, IEEE Trans. Geosci. Remote Sens. 62, 1-10, https://doi.org/10.1109/TGRS.2024.3357190 (2024).